

1 Supporting Information for

2 **Crust and Upper Mantle Structure Beneath the Eastern United States**

3 Chengping Chai¹, Charles J. Ammon², Monica Maceira¹, Robert Herrmann³

4 ¹Oak Ridge National Laboratory, Oak Ridge, Tennessee, U.S.A.

5 ²Department of Geosciences, Pennsylvania State University, University Park, Pennsylvania, U.S.A.

6 ³Department of Earth and Atmospheric Sciences, Saint Louis University, St. Louis, Missouri, U.S.A.

7
8
9
10 **Contents of this file**

11 Text S1

12 Figures S1 to S22

13
14
15 **Additional Supporting Information (Files uploaded separately)**

16 Caption for Dataset S1 to S2

17 Caption for Table S1

18 Caption for Movie S1

19 Caption for Visualization S1 to S2

20
21
22 **Introduction**

23 This supplement includes paragraphs describing cross-sections B1-B2, D1-D2, E1-E2, F1-F2, G1-
24 G2, and H1-H2 (Text S1); a figure showing the relative data variance of receiver functions (Figure
25 S1); a figure showing example surface-wave dispersions (Figure S2); a figure showing Bouguer
26 gravity maps before and after wavenumber filtering (Figure S3); a comparison of single-station
27 receiver functions and smoothed receiver functions (Figure S4); a figure showing the
28 convergence of the simultaneous inversion (Figure S5); a figure showing receiver function misfit
29 (Figure S6); a figure showing surface-wave dispersion misfit (Figure S7); a comparison of
30 observed gravity maps and predicted gravity maps (Figure S8); a comparison of EARS crust
31 thickness smoothing (Figure S9); a comparison of crustal thickness maps from recent seismic
32 velocity models (Figure S10); a figure showing the distributions of crustal and uppermost mantle
33 P-wave velocities (Figure S11); a comparison of upper mantle shear speed at 63 km depth in
34 western and eastern U.S. (Figure S12); maps showing cluster locations (Figure S13 and S15);
35 Velocity profiles for each cluster (Figure S14 and S16); a map showing locations of cross-sections

36 (Figure S17); V_s cross-section B1-B2 (Figure S18); V_s cross-section D1-D2 (Figure S19); V_s cross-
37 section E1-E2 and F1-F2 (Figure S20); V_s cross-section G1-G2 and H1-H2 (Figure S21); a
38 comparison of the uppermost mantle V_s and earthquake focal mechanisms (Figure S22); the
39 final seismic velocity model for the eastern United States in a text file (Data Set S1); the seismic
40 velocity model for the western United States in a text file (Data Set S2); a list of seismic
41 networks used in an excel file (Table S1); an animation compares the single-station-averaged
42 receiver functions and the smoothed version (Movie S1); and interactive tools to view the
43 seismic velocity model for the eastern United States (Visualization S1) and for the western
44 United States (Visualization S2).

45 **Text S1.**

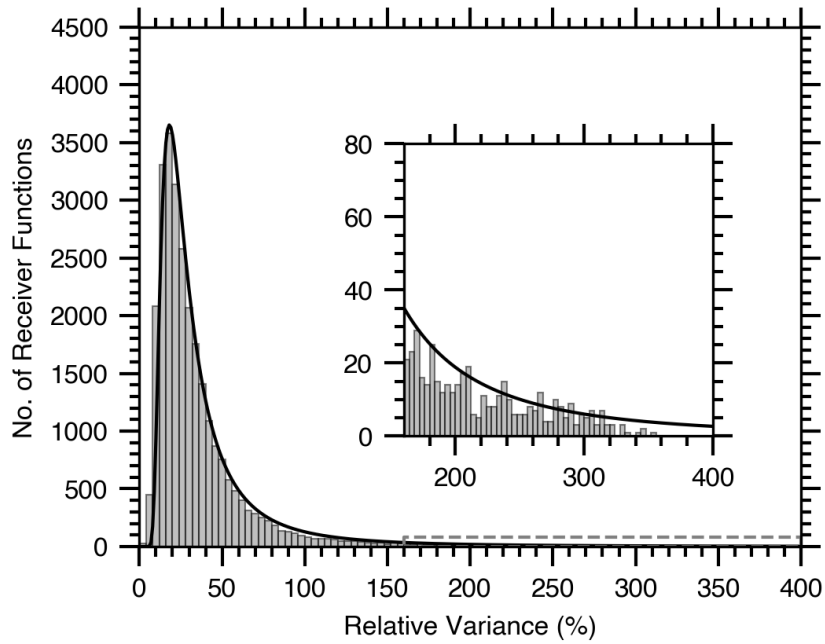
46 The cross-section B1-B2 (Figure S18) is parallel to the longer arm of the New Madrid
47 seismic zone (NMSZ) and passes through the Wabash Valley seismic zone (WVSZ) of
48 Illinois and Indiana. Compared to the region to the north (left in Figure), the crust hosting
49 modern WVSZ seismicity is relatively faster, with a smaller velocity gradient in the mid-
50 to-lower crust. The WVSZ is underlain by a slightly thicker crust than the NMSZ.
51 However, the upper mantle beneath the WVSZ is faster than that beneath the NMSZ. A
52 broad higher velocity anomaly is imaged beneath the WVSZ about 70-150 km depth,
53 which agrees with a recent local study (Chen Chen et al., 2016). The continuation of a
54 relatively fast lower crust beneath the NMSZ northward to the WVSZ may suggest these
55 two seismic active regions are connected (Chen Chen et al., 2016). To the south-
56 southwest of the NMSZ, deeper into the Mississippi Embayment, the sedimentary cover
57 thickens to at least 10 km and the crust thins to roughly 30 km.

58 The cross-section D1-D2, E1-E2, F1-F2, G1-G2, and H1-H2 pass through and across the
59 Appalachian Mountains. Cross-section D1-D2 (Figure S19) clearly shows a slower upper
60 mantle beneath New England, which is consistent with other studies (Pollitz & Mooney,
61 2016; Schmandt et al., 2015; Shen & Ritzwoller, 2016). The decrease seismic velocity
62 has been interpreted as due to interaction with the Great Meteor hotspot roughly 50 Ma
63 (Eaton & Frederiksen, 2007). Along the profile, which samples the Valley and Ridge
64 Province of central and eastern Pennsylvania, the crustal thickness increases by roughly
65 10 km from eastern Pennsylvania into the West-Virginia border. Crustal thicknesses in
66 western Pennsylvania are comparable to those to the south (see Figure 6). Although the
67 mid crust varies in speed along the profile, the change in crustal thickness appears to arise
68 from an increase in thickness of lower crustal material. Depths of earthquakes along the
69 profile are generally above 25 kilometers and show no systematic variation with the
70 structure.

71 Cross-section E1-E2 (Figure S20) samples from southeastern Canada into New England
72 and crosses the West Quebec seismic zone (WQSZ). Magnitude 3 and larger earthquakes
73 extend to 20 km depth in the WQSZ region and appear to shallow slightly along the
74 profile in New York and New England. Along this direction, the WQSZ locates near the
75 edge of the Canadian Shield as is evident in the mantle speed cross-section. Cross-section
76 F1-F2 (Figure S20) shows a crustal thickness change beneath central Pennsylvania.
77 Crossing from the Appalachian Plateau to the Valley and Ridge Province, the upper crust
78 slows and the lower crust thins. At roughly the same position the mantle speeds decrease.

79 Seismicity in the region shows transitions from reverse faulting in the thinner southeast
80 part of the state to strike-slip faulting in the northwest. Whether the stress change is
81 associated with the structure within the crust and/or upper mantle is difficult to tell. The
82 pattern of reverse faulting continues down the eastern seaboard along the area of
83 relatively thin crust. But reverse faulting in northern New York and southeastern Canada
84 occurs with crust with more typical interior thicknesses. The pattern is slightly better
85 matched with reverse faulting occurring above the regions of the relatively slow
86 uppermost mantle (see Figure S20), so perhaps the change (from South Carolina to
87 Ottawa) is a result of an overall variation in lithospheric strength.

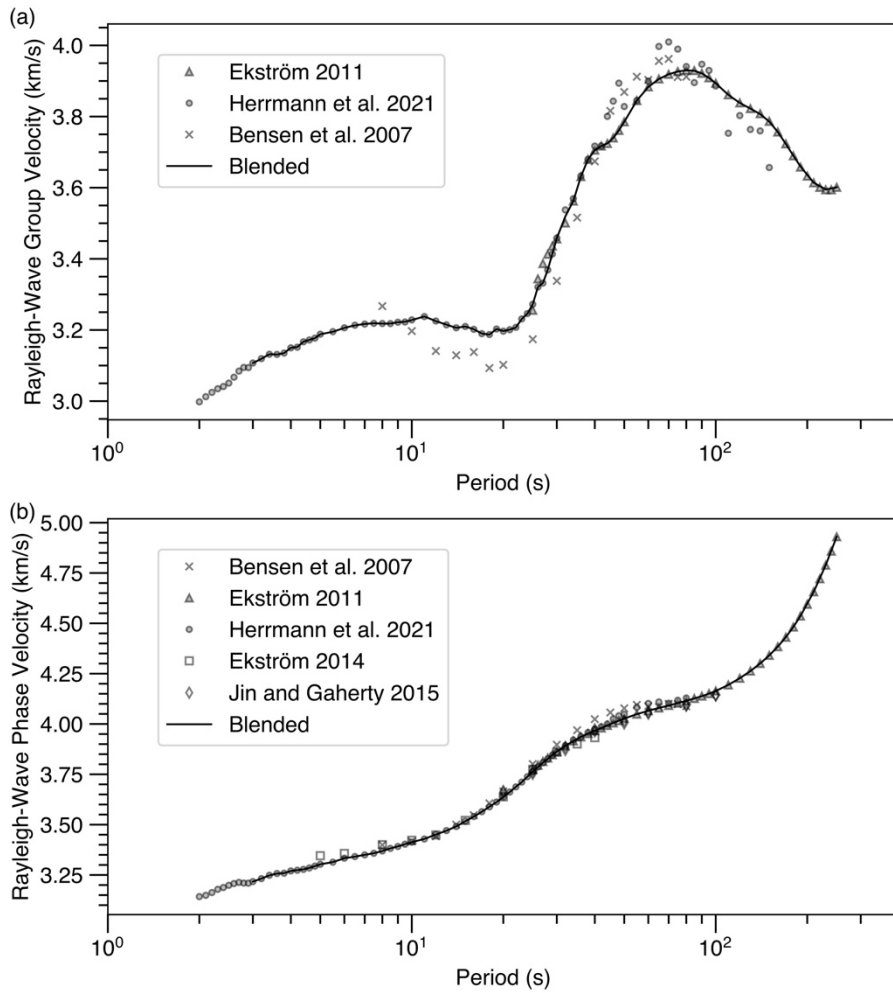
88 Cross-section G1-G2 (Figure S21) crosses eastern Ohio and through central Virginia and
89 into northwestern North Carolina. Crustal thickness in eastern Ohio is comparable to that
90 under the Appalachians, or perhaps slightly thinner. As discussed earlier in the Results
91 section, the crustal thickness changes quickly as you exit the Appalachians to the east.
92 Mantle speeds decrease modestly, but steadily from Ohio to the Appalachians. The 2011
93 M5.7 Virginia earthquake was located near an edge of a faster lower crust anomaly and a
94 change in crustal and upper mantle structure. Cross-section H1-H2 (Figure S21) crosses
95 from the northeast WVSZ to the Charleston region and the South Carolina Seismic Zone.
96 The crustal thickness increases slightly from the midwest into the Appalachians, and
97 seismicity appears to extend slightly deeper in the ETSZ near the profile. Near the
98 southeastern margin of the Appalachians, into the coastal plain, the depth range of slower
99 crustal material increases. The material that could be called lower-mid crust in the
100 midwest and Appalachians disappears as the material with typical lower-crustal speeds
101 shallows with a thinning of the crust. At the same position, the mantle speeds decrease
102 along the east coast. Mantle speeds decrease modestly, but steadily from Indiana to the
103 Appalachians, crossing the region that (Chu et al., 2013) suggested a hidden hot-spot
104 track. Along the profile, we see no evidence for a slow upper mantle. However, our
105 model includes a slight reduction in average upper mantle speed in northeast Kentucky
106 and southwest Ohio (see Figure 6), directly above the turning points of the rays that
107 showed delayed travel times and frequency-dependent amplitudes analyzed by (Chu et
108 al., 2013) (the signals were generated by the Virginia earthquake and recorded on
109 midwest Transportable Array (TA) stations described in that work). Our average is
110 shallower than where they placed the anomaly but may reflect the same feature.
111 However, we do not see it extend to the west, towards the northern Mississippi
112 Embayment, as they suggested.



113

114 **Figure S1.** Relative data variance distribution of receiver functions recorded in the Eastern U.S.
 115 region. The insets show a detailed view for relative variance ranges between 165% and 400%
 116 (dashed box). Black lines indicate extreme value distributions. The relative data variance is
 117 computed as the signal variance between an individual receiver function and the single-station-
 118 averaged receiver function.

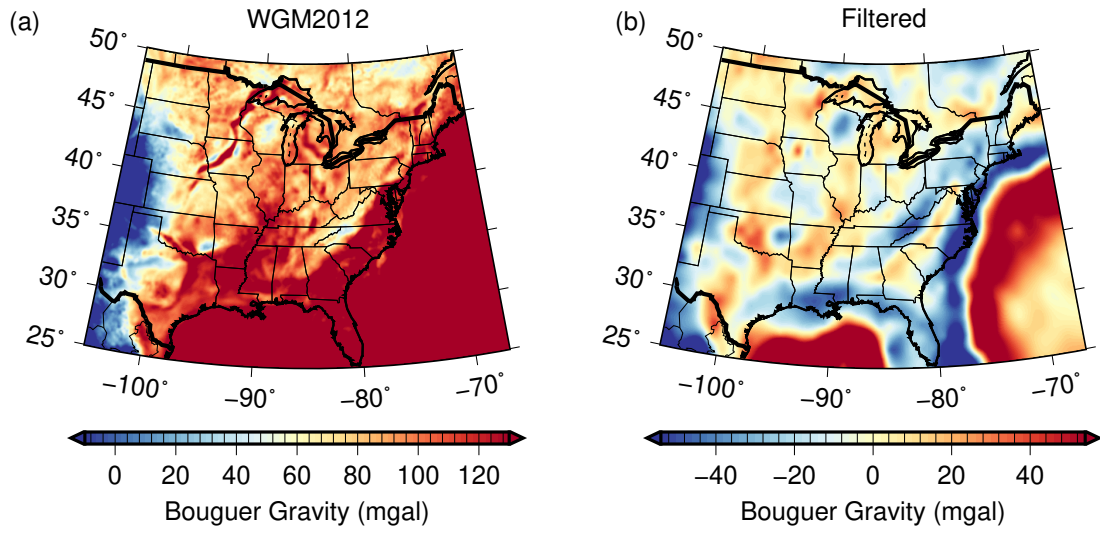
119



120

121 **Figure S2.** Example dispersion measurements and blended curves in the eastern U.S. (latitude
 122 44.5N, longitude 73.5E) for Rayleigh-Wave group velocity (a) and Rayleigh-Wave phase velocity
 123 (b). The blended curves were computed using values from Ekström (2011) and Herrmann et al.
 124 (2021). Dispersion models from other sources (Bensen et al., 2007; Ekström, 2014; Jin &
 125 Gaherty, 2015) are only shown for reference.

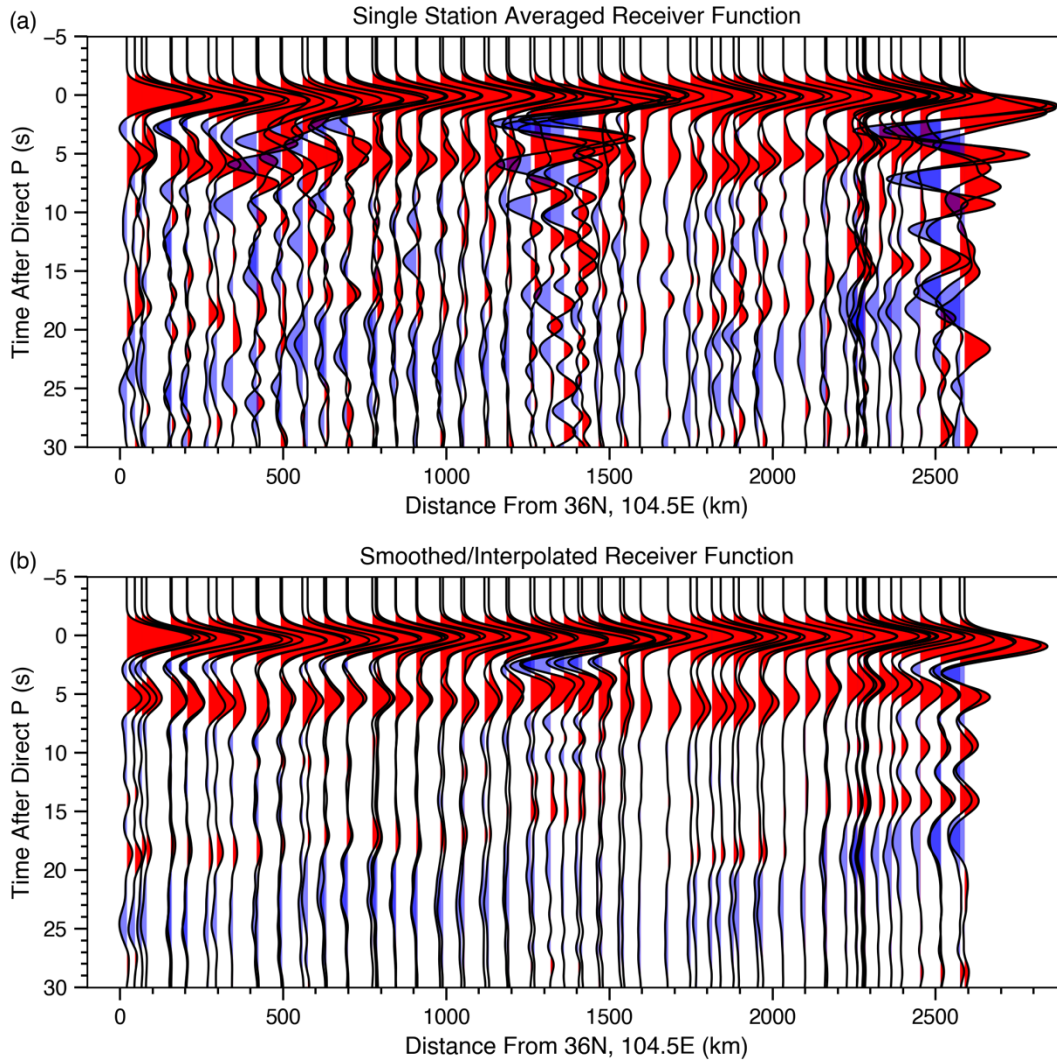
126



127

128 **Figure S3.** Bouguer gravity maps before (a) and after (b) wavenumber-filtering to emphasize
129 shallow structure and features have spatial dimension larger than 1° . Note the color scale
130 changes.

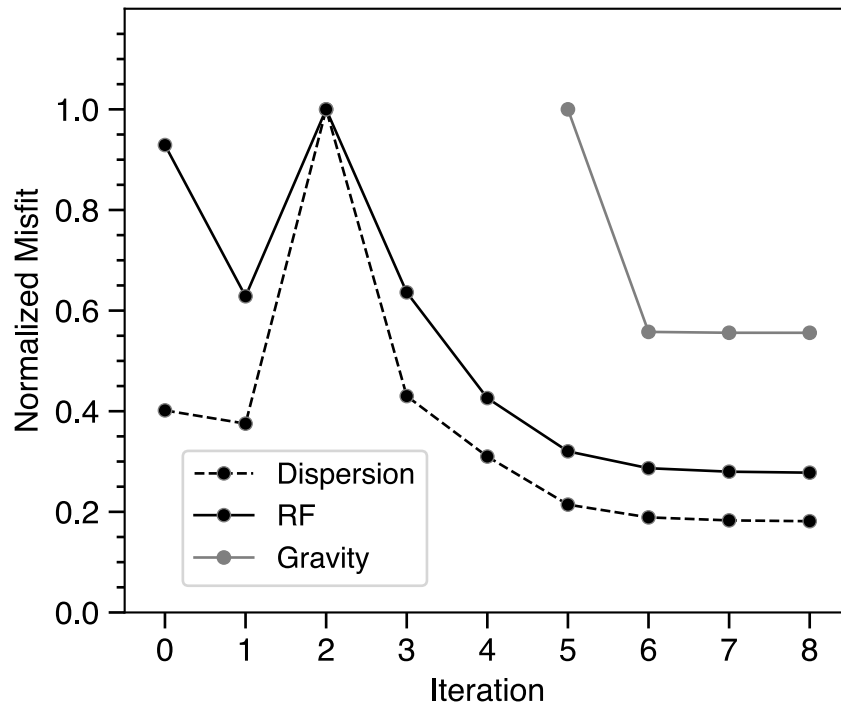
131



132

133 **Figure S4.** A comparison of (a) single station averaged and (b) smoothed/interpolated receiver
 134 functions in a cross-section view. The locations of the stations used are shown in Figure 1.

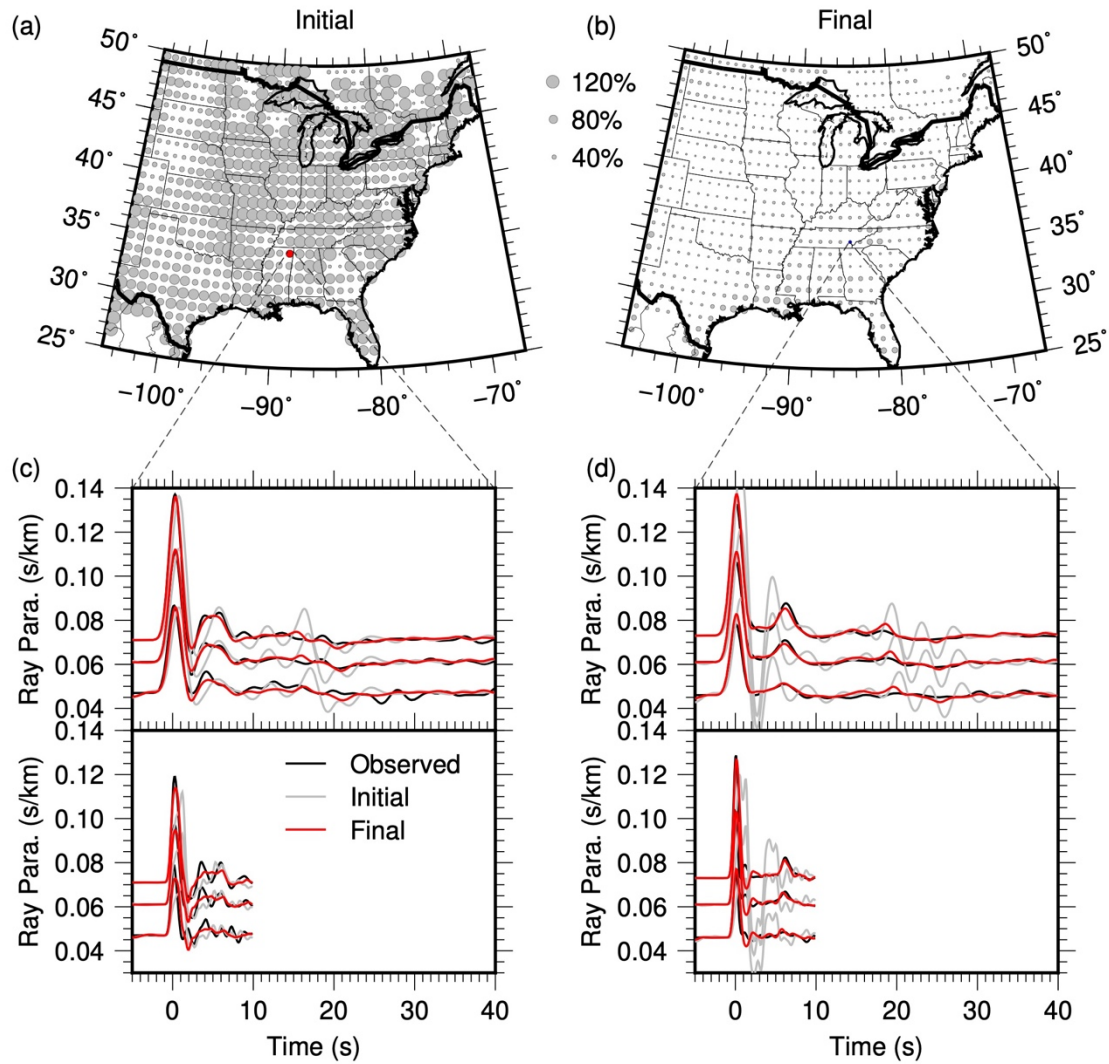
135



136

137 **Figure S5.** Convergence of the simultaneous inversion. The gravity observations were included in
 138 last three iterations. Misfits for each type of observations are normalized with the maximum.
 139 For each iteration, misfits were averaged over the grid. At each grid location, dispersion misfit
 140 was averaged between group and phase velocity measurements while receiver function misfit
 141 was averaged from all available receiver functions. RF stands for receiver function.

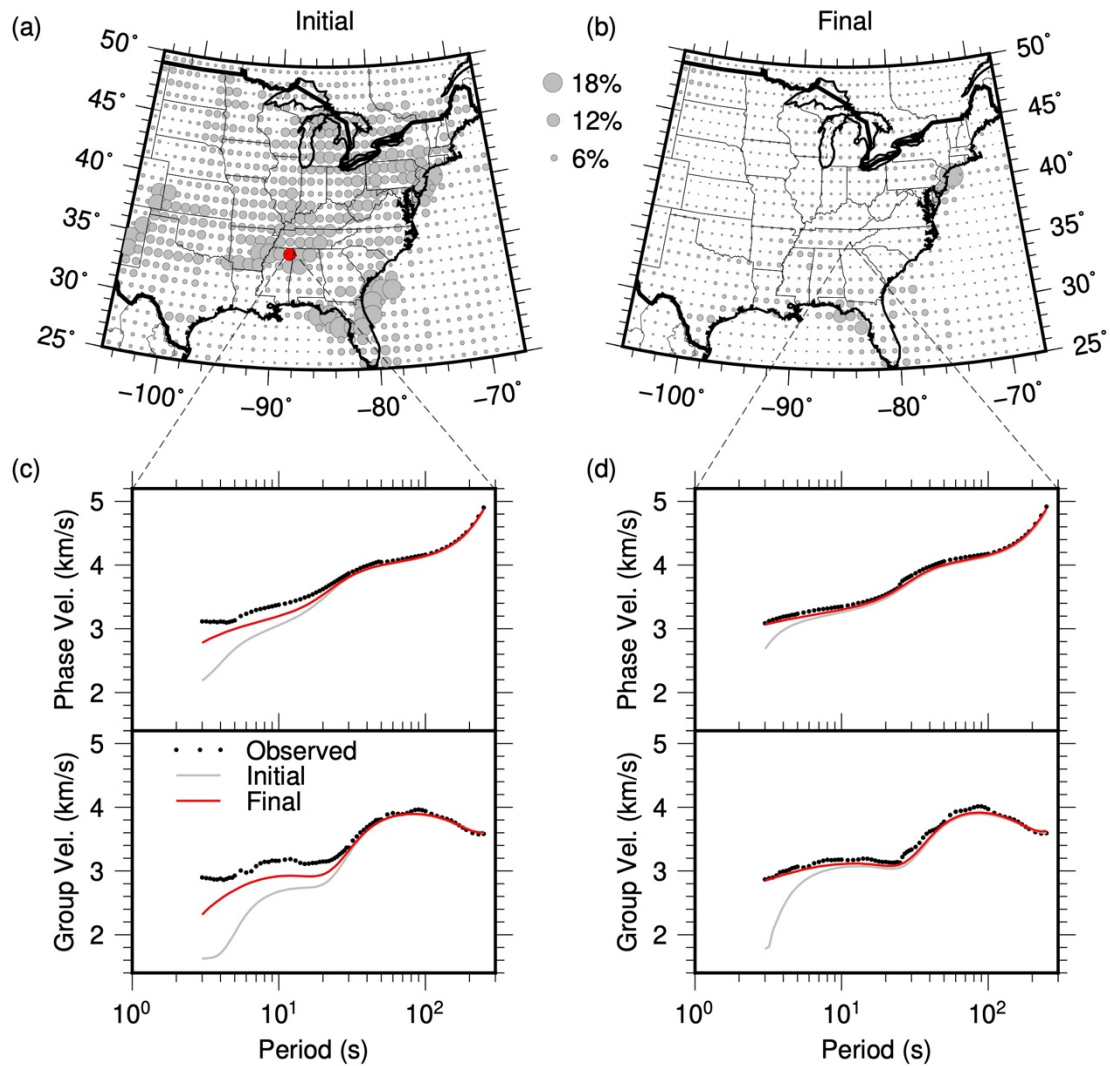
142



143

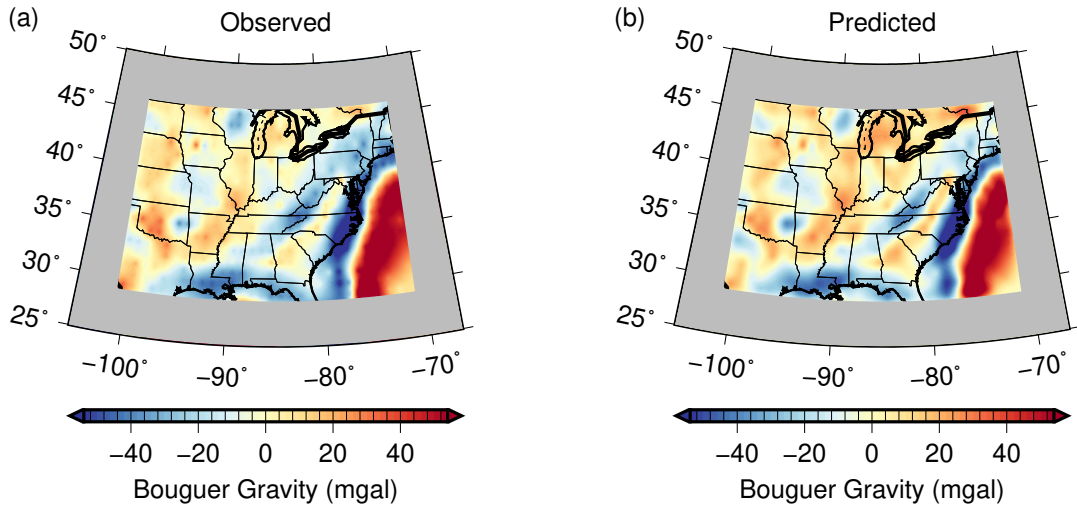
144 **Figure S6.** Receiver function misfit map for the initial model (a) and the inverted model (b). The
 145 size of dots represents the normalized misfit at each grid points. Receiver functions at two grid
 146 points (red and blue) are giving in (c) and (d) with the locations indicated by the dashed black
 147 lines. Receiver functions in different ray-parameter bins are displayed for both narrow-band
 148 (Gaussian 1.0, top frame) and broad-band (Gaussian 2.5, bottom frame). Since the broad-band
 149 receiver functions are noisier, we used a shorter time window.

150



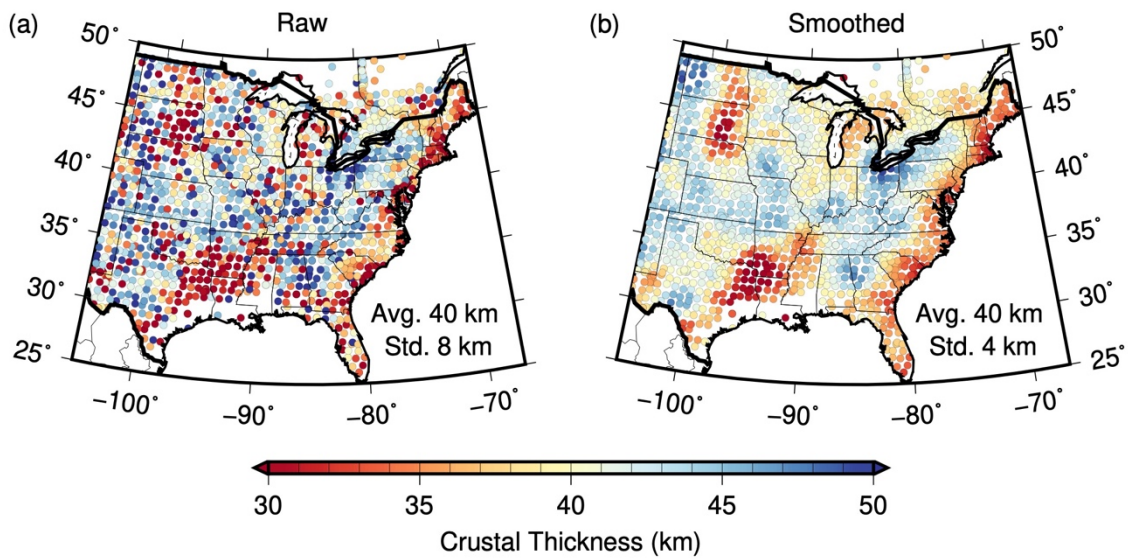
151

152 **Figure S7.** Surface-wave dispersion misfit map for the initial model (a) and the inverted model
 153 (b). The size of dots represents normalized misfit at each grid points. Rayleigh-wave dispersion
 154 curves at two grid points (34.5, -88.5) and (35.5, -84.5) (optimal and less-optimal data fits,
 155 respectively) are shown in (c) and (d) with the location indicated by the dashed black lines. The
 156 upper panel of (c) and (d) shows phase velocities while the lower panel shows group velocities.
 157



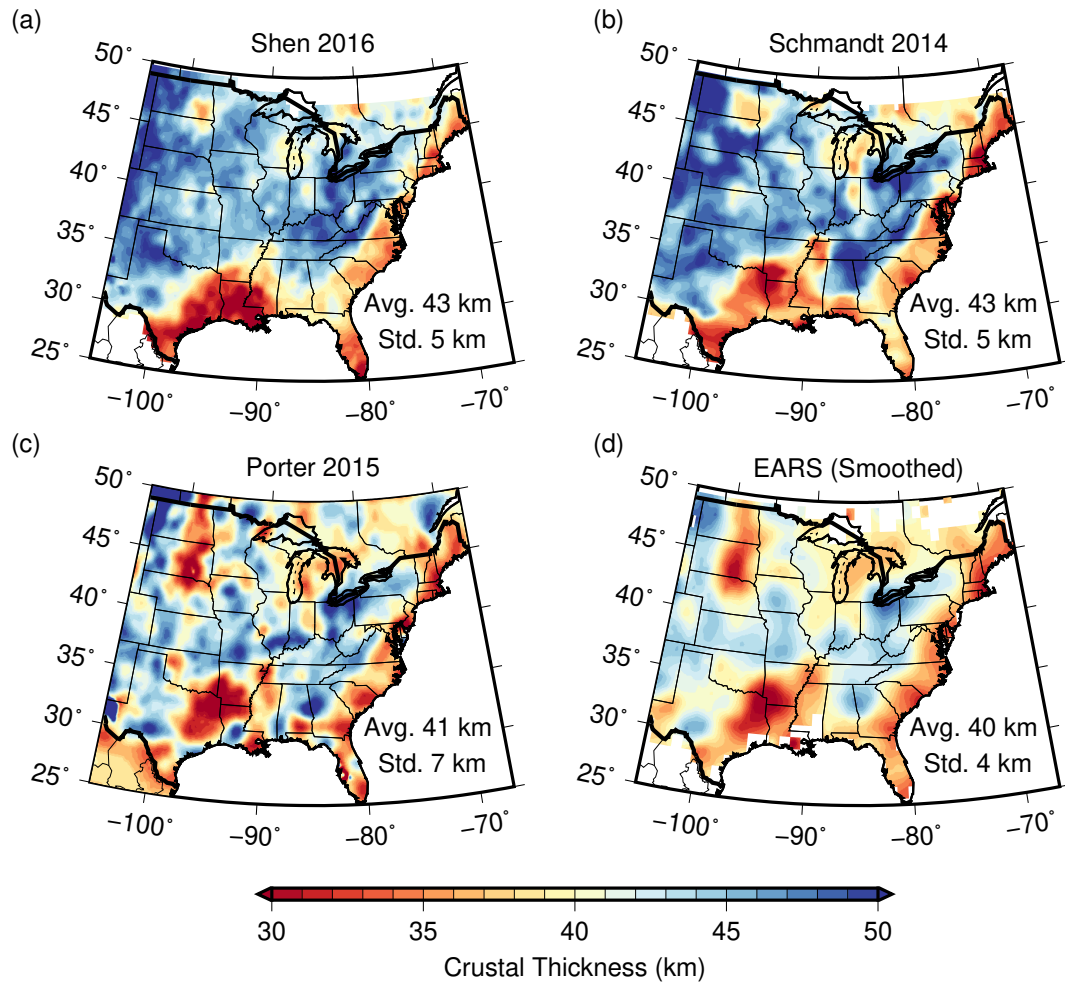
158

159 **Figure S8.** Comparisons of observed gravity maps (a) and predicted gravity maps (b) for the
 160 eastern U.S.



161

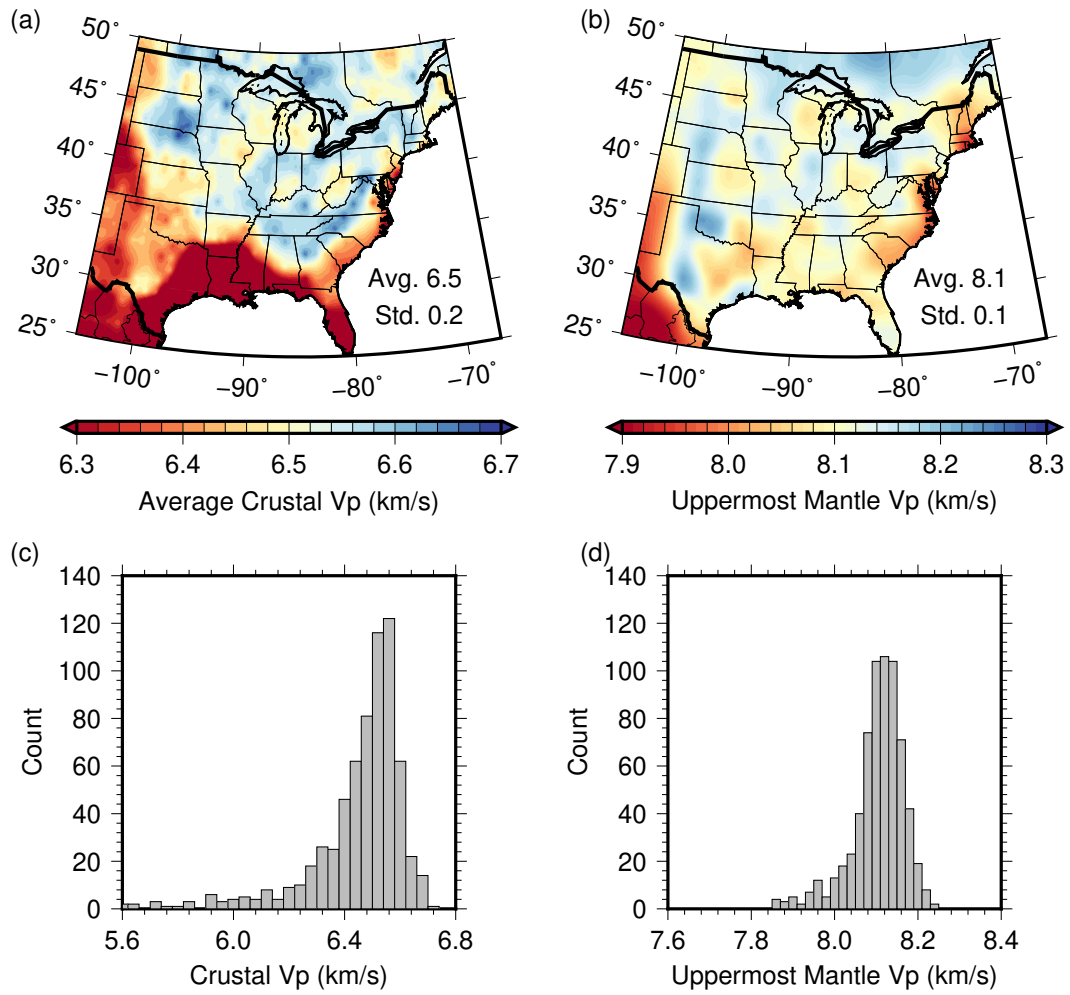
162 **Figure S9.** A comparison of EARS crustal thickness results (Crotwell & Owens, 2005) from the
 163 raw data (a) and the spatially smoothed version (b).
 164



165

166 **Figure S10.** A comparison of crustal thickness maps from four recent models, Shen-2016 model
 167 (Shen et al., 2016), Schmandt-2014 model (Schmandt et al., 2015), Porter-2015 model (Porter et
 168 al., 2016), and EARS model (Crotwell & Owens, 2005). The results of this paper are shown in
 169 Figure 5.

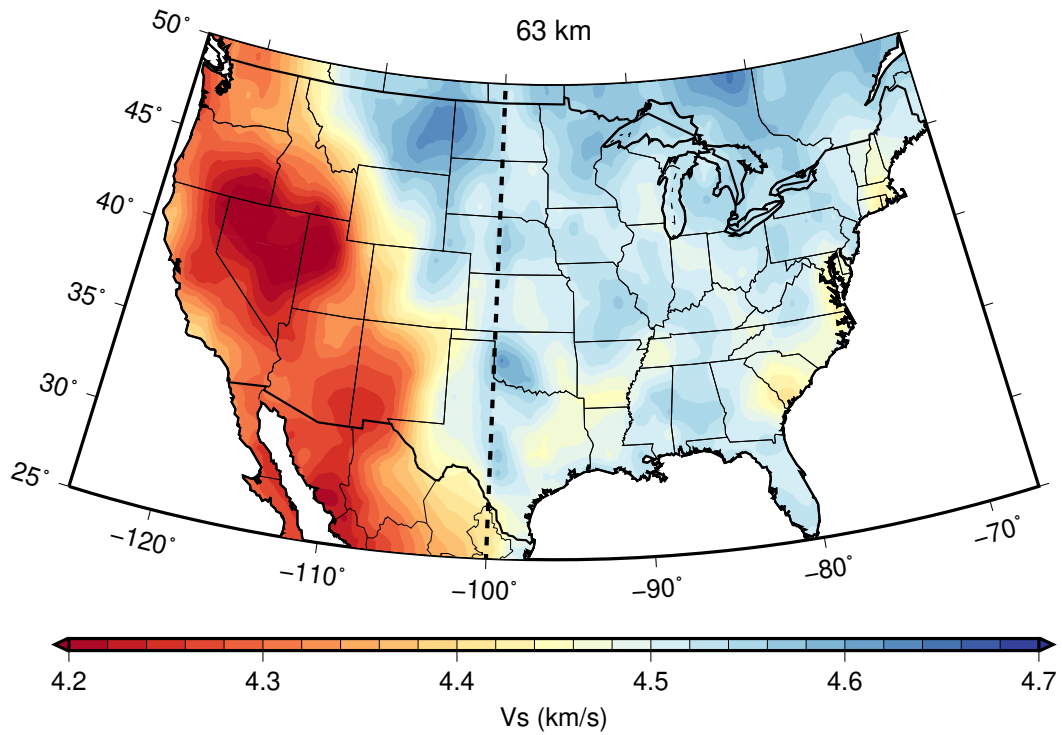
170



171

172 **Figure S11.** Average crustal Vp speed map, uppermost mantle Vp speed map and histograms of
 173 crustal and uppermost mantle Vp velocity.

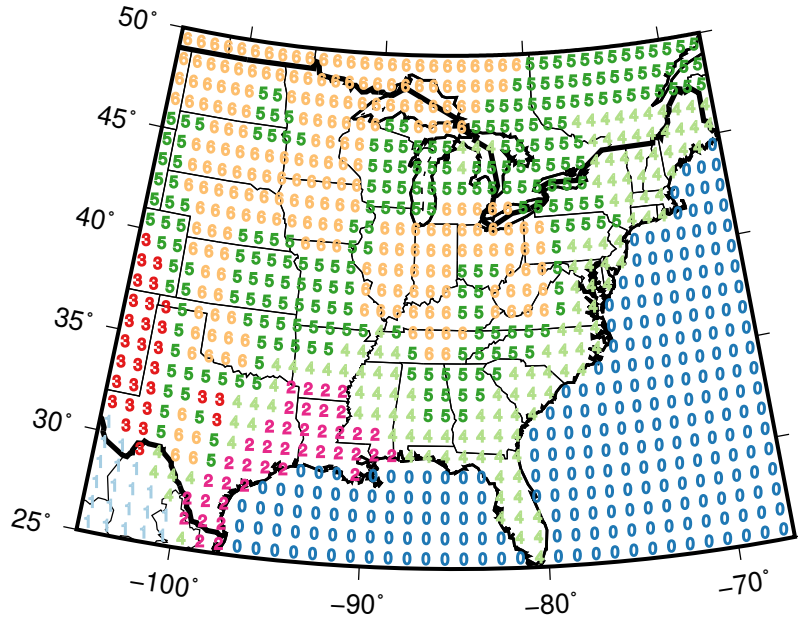
174



175

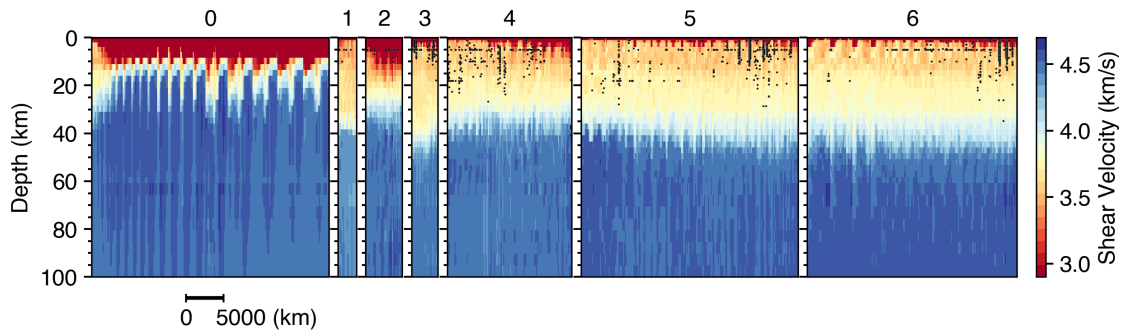
176 **Figure S12.** A comparison of upper mantle shear speed at 63 km in western and eastern U.S. The
 177 dashed line indicates the transition from the western U.S. model (Chai et al., 2015) to the
 178 eastern U.S. model (this study).

179



180

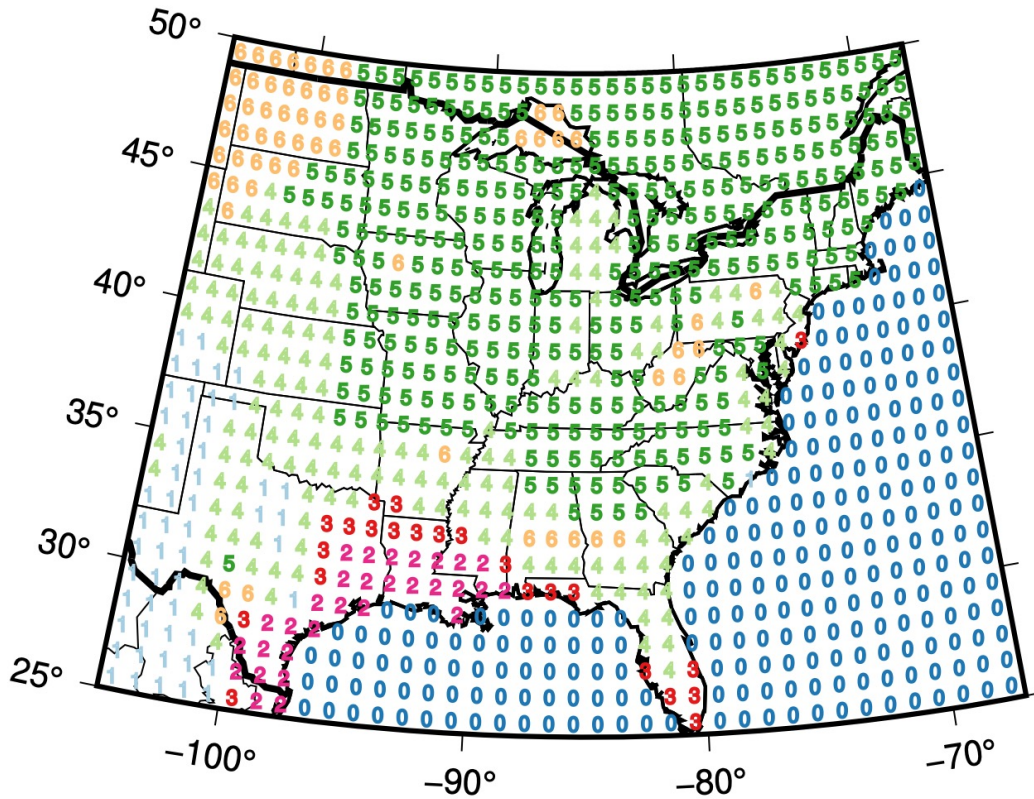
181 **Figure S13.** Locations of the automated model clusters generated using a simple hierarchical
 182 clustering algorithm. The shear velocities between 6 km and 200 km in depth was used for the
 183 clustering. Note the oceanic profiles were assigned based on location. The rough
 184 correspondence of the clusters to geologic regions are (0) Oceanic; (1) Southern Basin and
 185 Range Region; (2) Western Mississippi Embayment; (3) Central Basin and Range Region; (4)
 186 Atlantic Plain and Northern Appalachian Highlands; (5) and (6) Interior Plains, Central and
 187 Southern Appalachian Highlands, and Southern Canadian Shield. The velocity profiles within
 188 each cluster are summarized in Figure S14.



189

190 **Figure S14.** Shear velocity profiles of Earth model clusters constructed using a hierarchical
 191 clustering algorithm. The shear velocities between 6 km and 200 km in depth was used for the
 192 clustering. The label above each panel correspond to that in Figure S13. Southern regions are
 193 shown on the left, regions from the interior of North America toward the right. Velocity profiles
 194 within the cluster are sorted from north to south by row (like in a book). Dots shows seismicity
 195 (magnitude 3 and larger) from the USGS NEIC catalog before May 2021.

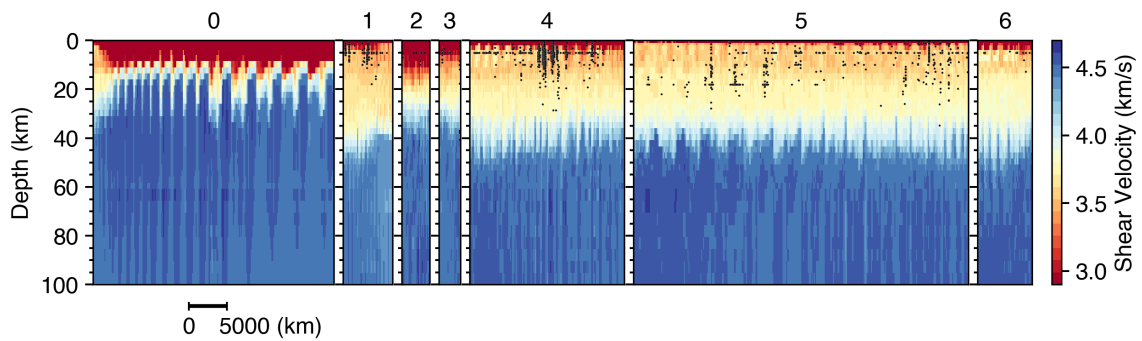
196



197

198 **Figure S15.** Same as Figure S13 but used the shear velocities of the upper 20 km. Similar to
 199 Figure 11 from Herrmann et al. (2021), this figure can be used to select a 1D local model for
 200 further analysis.

201

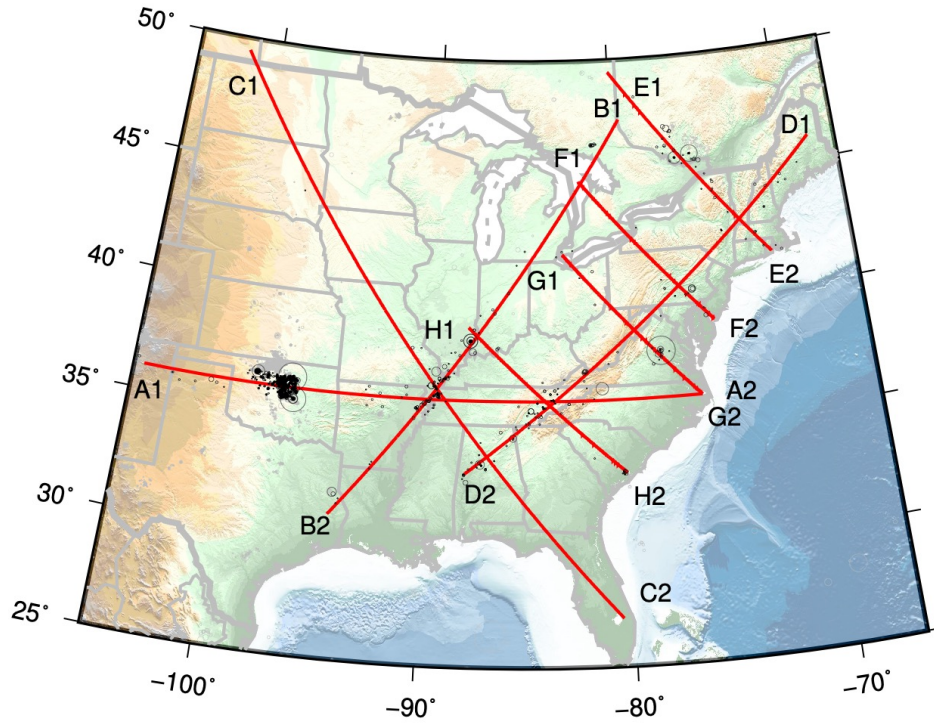


202

203 **Figure S16.** Same as Figure S14 but the clustering used the shear velocities of the upper 20 km.
 204 The label above each panel correspond to that in Figure S15.

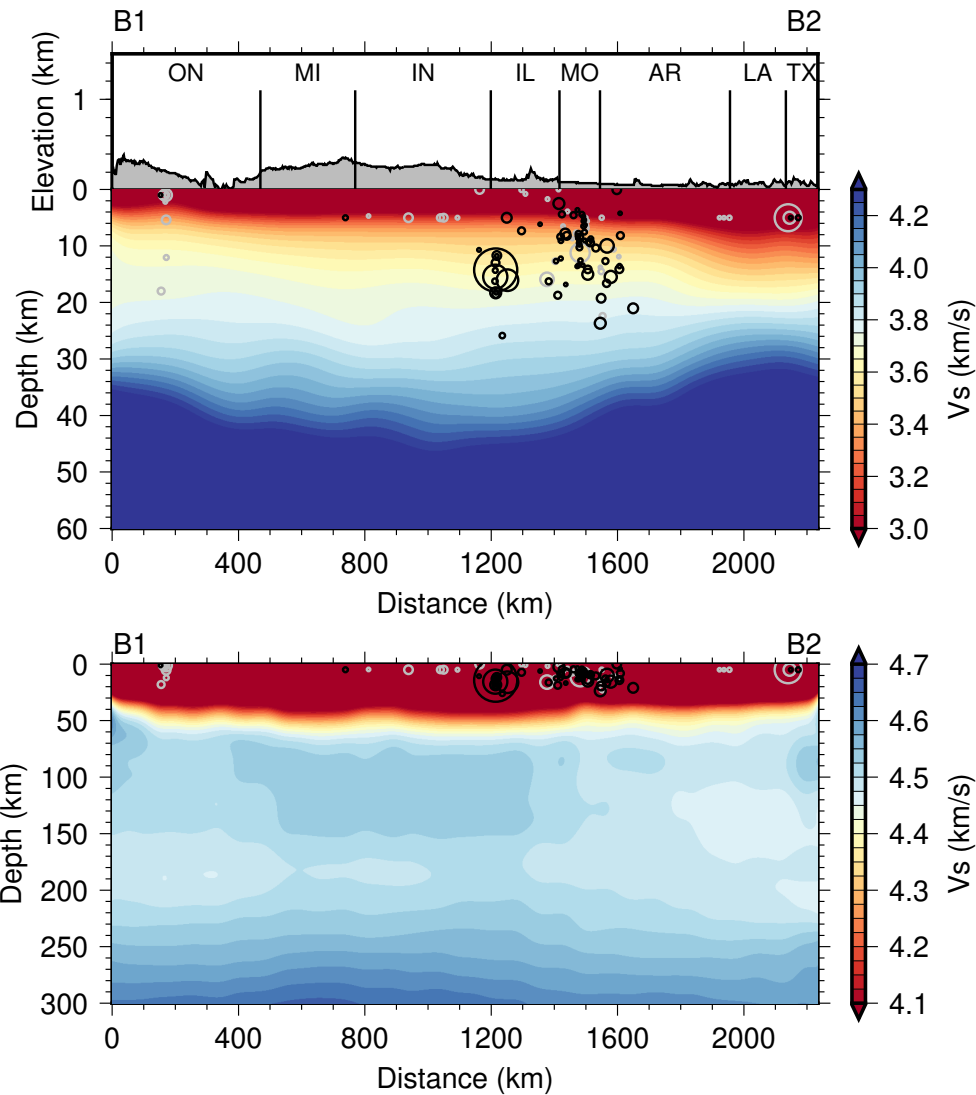
205

206



207

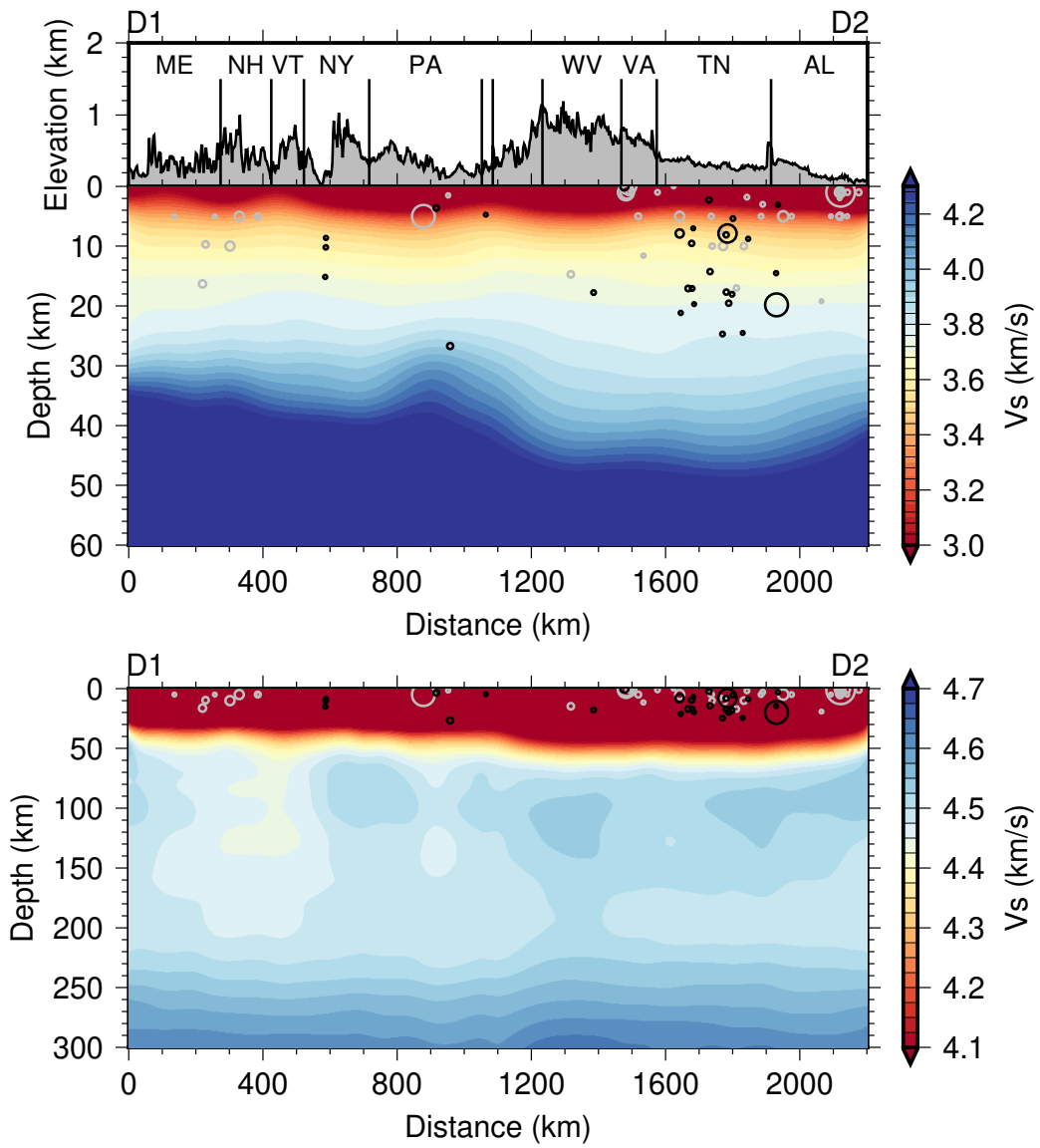
208 **Figure S17.** Seismicity (black and gray circles, magnitude 3 and larger prior May 2021) and cross-
 209 section locations (red lines). Black circles represent earthquakes that are shown in cross-
 210 sections. Gray circles are earthquakes that located 100 km away from any cross-sections. Larger
 211 circles correspond to larger magnitudes. The earthquake data were downloaded from USGS
 212 NEIC catalog.
 213



214

215 **Figure S18.** Shear velocity cross-sections along B1-B2. Top panel used a color palette for suitable
 216 for crustal speeds. The lower panel shows shear-wave velocity changes in the upper mantle.
 217 Circles are earthquakes located within 100 km of the cross-section. Black circles are events with
 218 depth uncertainties less than 5 km. Gray circles represent earthquakes with larger depth
 219 uncertainties or without uncertainties. Note the image is vertically exaggerated.

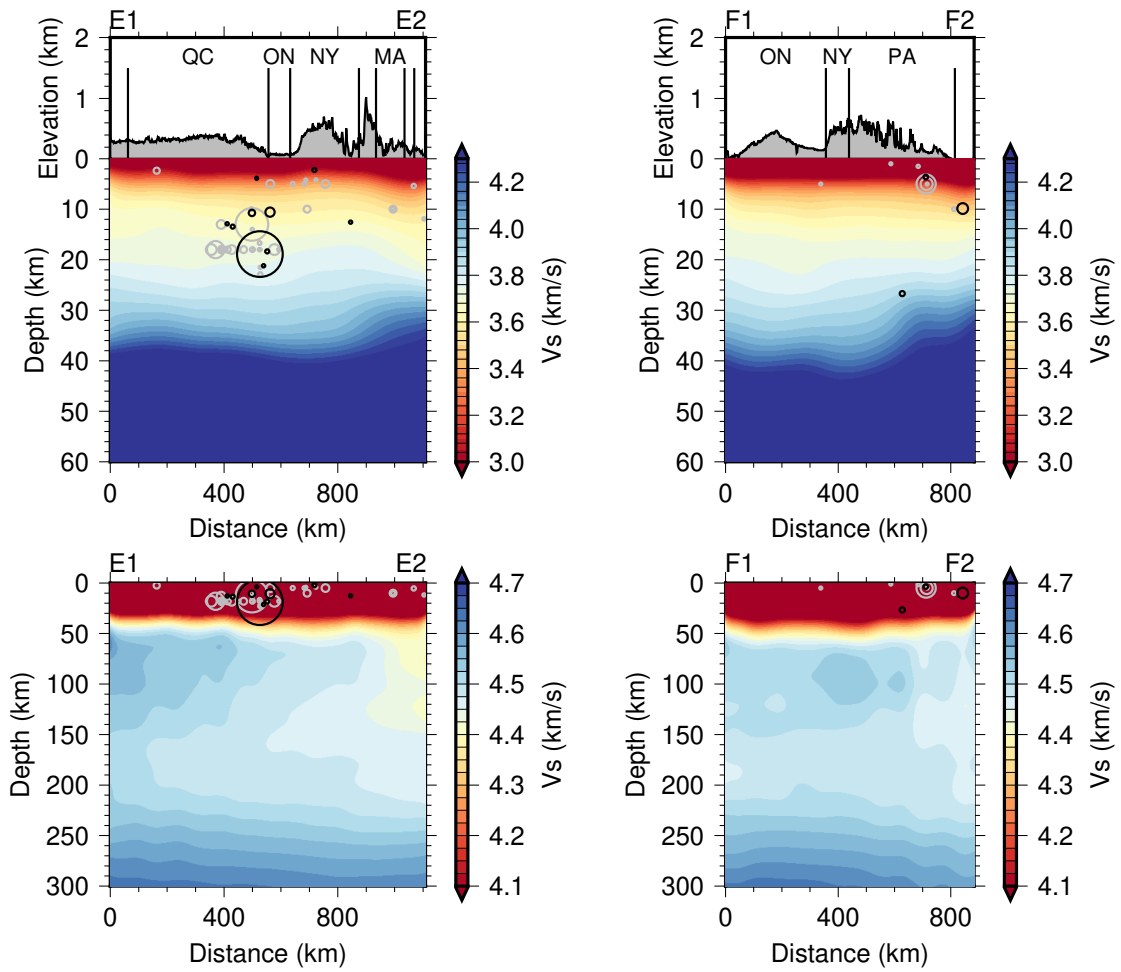
220



221

222 **Figure S19.** Same as Figure S18 but for cross-section D1-D2.

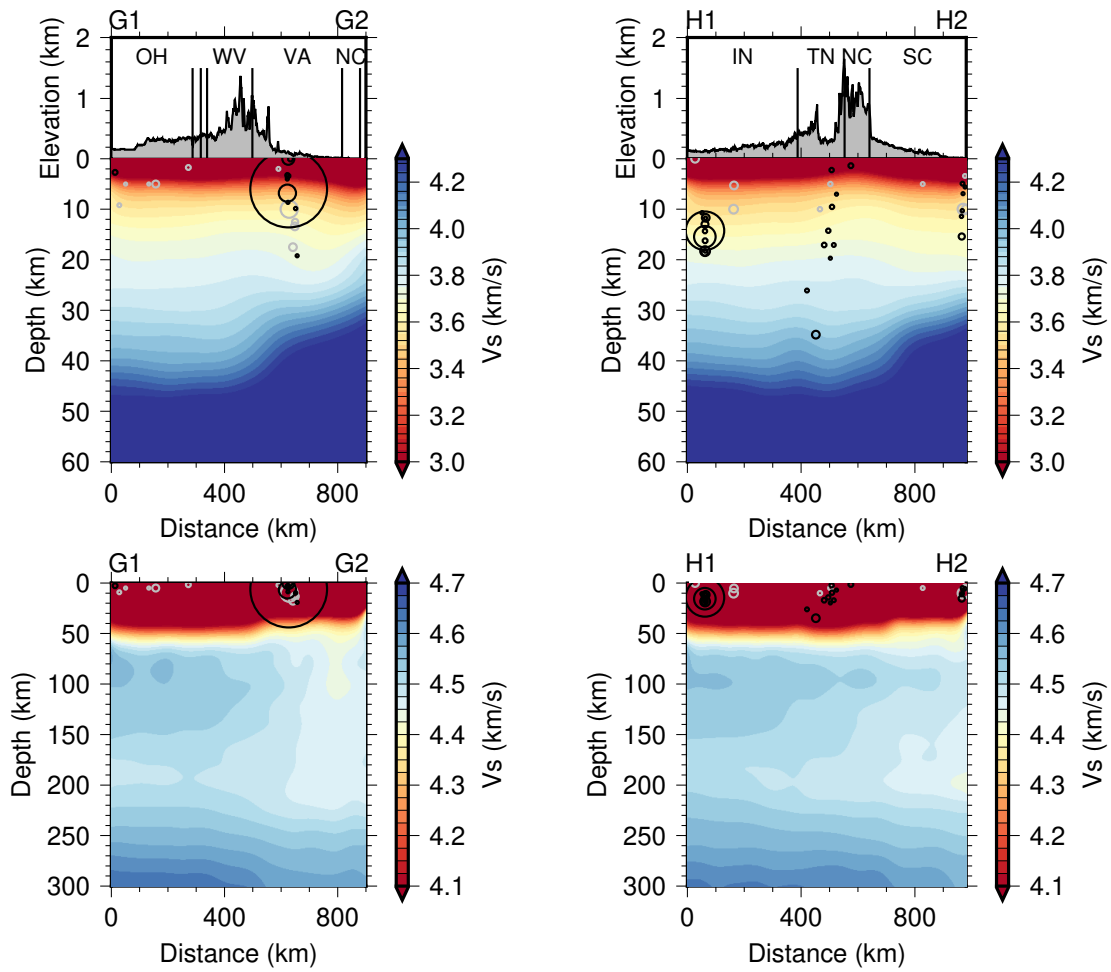
223



224

225 **Figure S20.** Same as Figure S18 but for cross-sections E1-E2 and F1-F2.

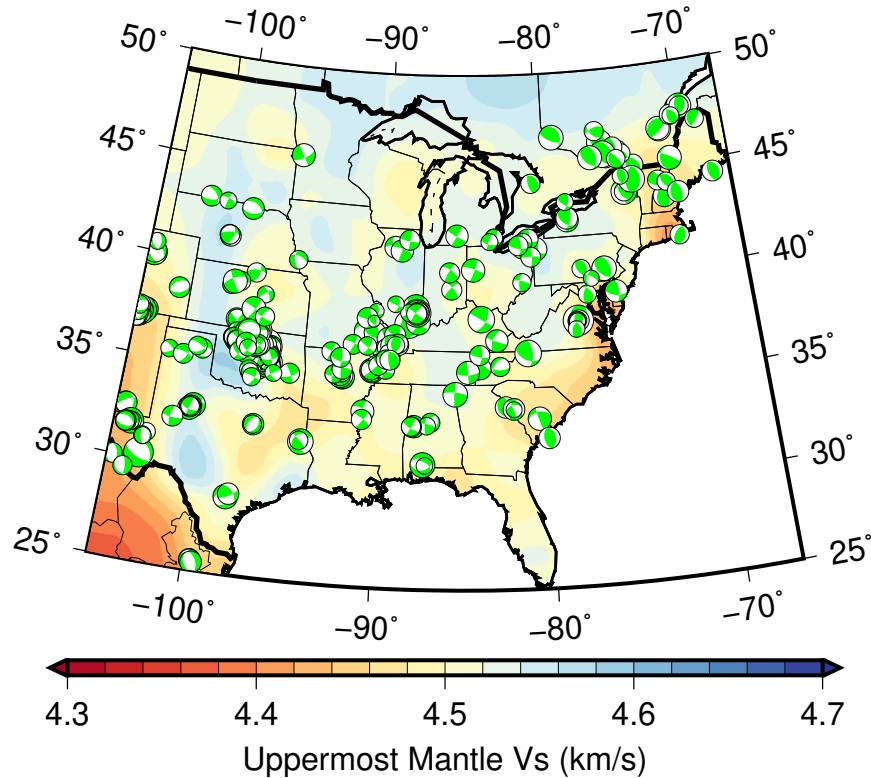
226



227

228 **Figure S21.** Same as Figure S18 but for cross-section G1-G2 and H1-H2.

229



230

231 **Figure S22.** A comparison of the uppermost mantle V_s and focal mechanisms from the Saint
 232 Louis University (SLU) catalog (prior 2021/05/01).

233

234 **Table S1.** A list of seismic networks used for the receiver function calculation.

235

236 **Data Set S1.** The final seismic velocity model for the eastern United States derived from the
 237 inversion. The first column is latitude. The second column is longitude. The third column is depth
 238 (top of the cell) in kilometers. The fourth, fifth and sixth column are P-wave velocity (km/s), S-
 239 wave velocity (km/s), and density (g/cm^3), respectively.

240

241 **Data Set S2.** The seismic velocity model for the western United States from Chai et al. (2015).
 242 The first column is latitude. The second column is longitude. The third column is depth (top of
 243 the cell) in kilometers. The fourth, fifth and sixth column are P-wave velocity (km/s), S-wave
 244 velocity (km/s), and density (g/cm^3), respectively.

245

246 **Movie S1.** An animation compares the single-station-averaged receiver functions against the
 247 spatially smoothed/interpolated receiver functions.

248

249 **Visualization S1.** An interactive tool to view S-wave velocities of the 3D model for the eastern
250 United States as depth slides and depth profiles side by side. The visualization was created with
251 a Python script developed by Chai et al. (2018).

252

253 **Visualization S2.** An interactive tool to view S-wave velocities of the 3D model for the western
254 United States (from Chai et al., 2015) as depth slides and depth profiles side by side. The
255 visualization was created with a Python script developed by Chai et al. (2018).

256

257